

X-Ray Backlighting of Shock Ignition Experiments on the National Ignition Facility

Thomas Mo

Webster Schroeder High School

LLE Advisor: **Dr. R.S. Craxton**

Laboratory for Laser Energetics

University of Rochester

Rochester, New York

November, 2010

Abstract:

A computer code *Blackthorn* has been written to model the radiography of an imploding fusion target using an x-ray backlighter. *Blackthorn* traces x rays from the backlighter source through the target to a camera, which is at an arbitrary viewing angle. *Blackthorn* can model the target at any specified time and x-ray energy, drawing a contour plot that imitates an actual image produced by an x-ray backlighter, including self-emission, from the perspective of the viewing position. Input files from a computer code SAGE, which contains a 3D grid of center of mass radius, are combined with input files from another code, LILAC, which contains 1D profiles of mass density and electron temperature versus radius, to produce a 3D representation of the target density. The capabilities of *Blackthorn* are illustrated by application to a fusion target proposed for shock-ignition polar-drive experiments on the National Ignition Facility (NIF). A view from the polar position can be used to diagnose the azimuthal uniformity of the target, while a view from the equator can be used to diagnose the balance of compression between the polar and equatorial positions. *Blackthorn* is being used to help design and optimize x-ray backlighting diagnostics for the proposed experiments. Using 1D line-plots created by *Blackthorn*, 3500eV has been determined as an optimal frequency to view backlighting images.

1. Introduction:

Fusion is the process through which two or more nuclei fuse together to form a single heavier nucleus. Normally, fusion creates a more stable nucleus and results in the release of a large quantity of energy. To achieve fusion, the nuclei must be at a high density and temperature. These conditions will increase the number of collisions between the nuclei and

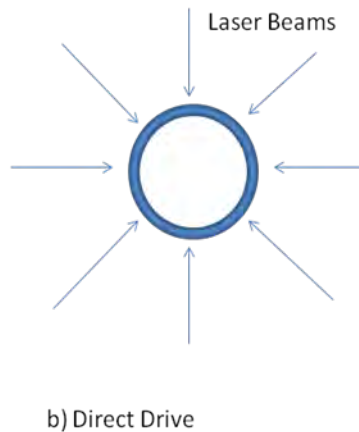
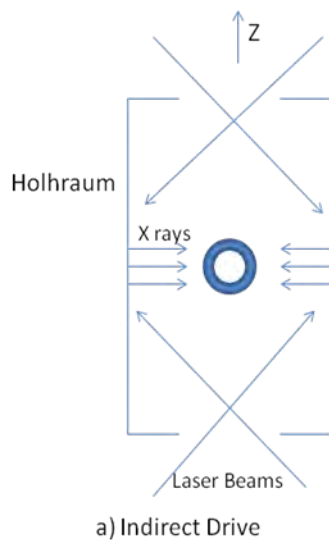


Figure 1: Two types of laser fusion. (a) In indirect drive fusion, laser beams strike the inside of a hohlraum, which then emits x-rays to irradiate a spherical fuel capsule. (b) In direct drive fusion, the laser beams directly and uniformly irradiate the capsule from all incident angles.

increase their kinetic energy, so that the nuclei will overcome their repulsive electrostatic forces in favor of their attractive nuclear forces and fuse together. In hydrogen fusion, a deuterium nucleus fuses with a tritium nucleus to create a helium nucleus and a neutron with a large amount of energy. Applying this concept to a spherical fuel capsule

consisting of a thin plastic shell filled with deuterium and tritium, fusion reactions can be carried out. These fusion reactions can provide a means of creating a future source of energy. The conditions for fusion can be met by using high-energy lasers to strike the capsule. The lasers deposit energy on the outside of the capsule so the outside ablates and the inside implodes. If the implosion is uniform and the conditions are met, fusion will occur.

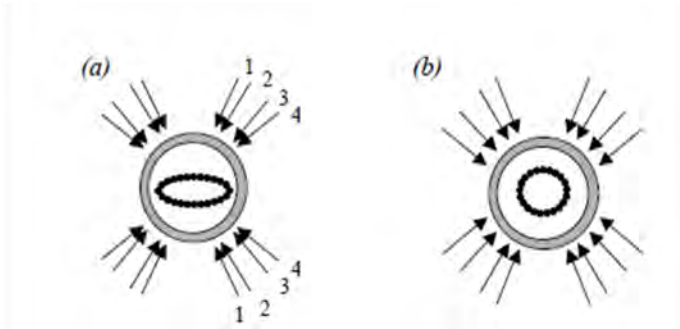


Figure 2: Two types of NIF beam pointings: direct drive and polar direct drive. (a) In direct drive, the target increases in non-uniformity as it implodes when the laser beams are initially pointed at the target center. (b) In polar direct drive, the beams are pointed away from the center, to improve the overall implosion uniformity. (from Ref. 5)

from the top and bottom, which then emits x-rays to irradiate the fuel capsule, located at the center of the cylinder. The National Ignition Facility (NIF) in Livermore, California is built for and currently specializes in indirect drive experiments. The NIF uses 192 beams of lasers organized into 48 quads (set of four lasers), in which all are designed to irradiate the inside of the hohlraum wall from the top and bottom. The quads are located at angles of 23.5, 30, 44.5, and 50 degrees to the z axis above and below the equator. On the other hand, in direct drive fusion, the laser beams directly and uniformly irradiate the target from all incident angles. Since the NIF facility has no equatorial beams, as it was constructed primarily for indirect drive experiments, polar direct drive^{3,4} has been designed to enable direct drive experiments to be performed on the NIF. In polar direct drive, the beams maintain their indirect drive port configurations, but are re-pointed from the center of the target to achieve the best uniformity after compression (Fig. 2).

Currently, there are two main types of direct drive that may provide a path to attaining fusion energy in the future: hotspot ignition and shock ignition. Hotspot ignition⁶ consists of the simultaneous heating and compression of the target center to start fusion in the center. Once fusion is present in the center, alpha particles (helium nuclei) will propagate outward and heat the fuel, creating a chain reaction. However, compressing a target full of "hot fuel" is very difficult, so an alternative technique, called shock ignition, has been proposed (Fig. 3). Shock

There are two ways to implode the target with lasers: indirect drive fusion¹ and direct drive fusion² (Fig. 1). Indirect drive fusion involves laser beams striking the inside of a hohlraum, a metallic cylinder through which the laser beams enter

ignition^{8,9} contains two steps. In the first step, the “cold fuel” is compressed at low velocity, represented by the portion of the red curve with lower power (P_{main}) in Fig. 3. In the second step, a powerful laser pulse, represented by the P_{shock} portion of the red curve, is used to launch a short, strong, spherically convergent shock on the outside of the target. The shock propagates inward, and the focused energy heats the center rapidly to generate fusion. Shock ignition can only be performed with direct drive because

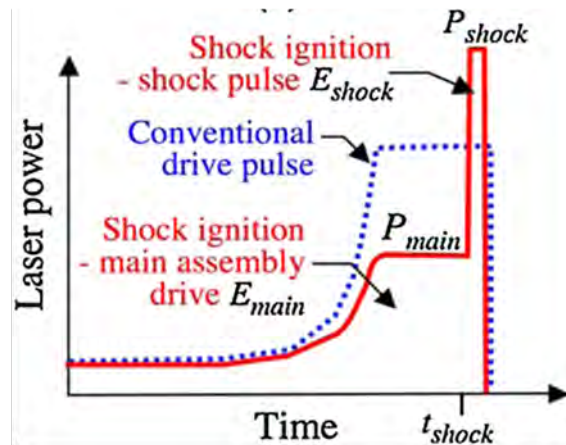


Figure 3: A graph comparing conventional hotspot ignition (blue) and shock ignition (red). The shock-ignition pulse has a drive pulse with power P_{main} followed by a shock pulse with power P_{shock} . (from Ref. 7)

the short laser pulse cannot heat the holhraum to a high enough temperature rapidly enough.

Perkins has proposed to test polar direct drive shock ignition on the NIF⁷. Half of NIF's beams, 96 main beams, are used to form the compression pulse and the other half, the 96 igniter beams, are used to form the shock pulse⁷. During the first part of the experiment, only the compression step is proposed to see if the fuel capsule, also referred to as the target, can be compressed sufficiently and uniformly using only half of the NIF beams. Tucker¹⁰ has developed a design for this compression stage, but since this design and future designs may not produce perfect uniformity in compression, x-ray backlighting is needed to diagnose the uniformity, which is vital to achieving fusion. For x-ray backlighting, some laser beams not used to irradiate the target strike an x-ray source and create a layer of plasma (Fig. 4). The layer of plasma then emits x-rays which pass through the target, and those rays that pass through the pinhole and onto the x-ray detector create the backlighting image.

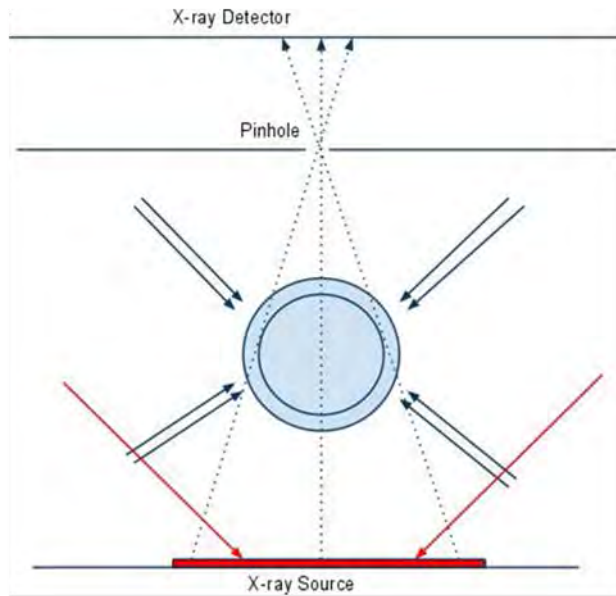


Figure 4: A diagram representing a proposed x-ray backlighting system for the NIF. The blue arrows represent laser beams used to compress the target in the center. The red arrows represent laser beams used to power the x-ray source. The red layer represents the plasma created from lasers striking the source. X-rays that pass through the pinhole create an image of the target on the detector. In reality, the target is much smaller than depicted, so the x-rays travel almost in parallel to each other.

Unfortunately, NIF shots are exceedingly limited; the system is capable of shooting up to three times per day, but presently the NIF only shoots once per day. Therefore, simulations of x-ray backlighting must be completed before the actual experiment is carried out. Tucker's design, obtained using the code SAGE¹¹, can

provide predictions of the 3D target shell, but prior to this work the capability to simulate the x-ray backlighting image of the 3D object did not exist. This work describes a computer code *Blackthorn* that has been written to predict the image seen by an x-ray detector from any detector angle relative to the capsule.

2. X-ray Propagation in *Blackthorn*:

2.1: Theory

For an x ray of frequency ν moving along a path whose position is measured by its distance of travel s , (Fig. 5(a)), its spectral intensity I_ν is given by the equation of radiation transfer¹²:

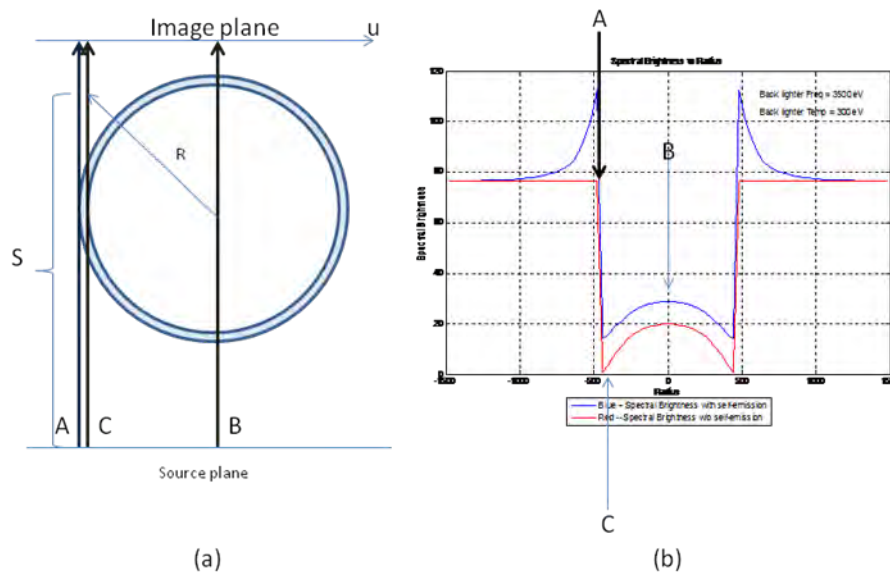


Figure 5: (a) A diagram indicating x-ray paths through a target and (b) graphs of spectral intensity vs. radius in the image plane produced by *Blackthorn* with self emission (blue) and without self-emission (red). The ring in (a) represents the target shell. For an x-ray of distance s along its path, it is at a radius R from the target center. The opacity is high in the ring and very low everywhere else. There is almost nonexistent attenuation for the path starting at A, intermediate at B, and high at C.

$$\frac{dI_\nu}{ds} = -k'_\nu I_\nu + k'_\nu B_\nu \tag{1}$$

where k'_ν is the opacity and B_ν is the blackbody spectral intensity evaluated at the local temperature. The first term on the right hand side depends on I_ν , where $I_\nu * ds * d\Omega * dt * d\nu$ equals the energy crossing a x-ray receiving area ds , $d\nu$ is the frequency interval of the x ray, $d\Omega$ is the

solid angle, and dt is the time interval. The second term depends on B_ν , the blackbody spectral intensity of the target given by Planck's law¹²:

$$B_\nu(T) = \frac{(2h\nu^3)}{c^2} * \left(\frac{1}{e^{\frac{h\nu}{kT}} - 1} \right) \quad (2)$$

where h is Planck's constant, ν is the x-ray frequency, c is the speed of light, k is Boltzmann's constant, and T is the local temperature. Eq. 2 shows that B_ν is only a function of the x-ray frequency and the local temperature at the x-ray position.

In Eq. (1), the first term represents absorption and the second term represents self-emission. Since B_ν is a function of temperature, if it is assumed that $T=0$ so that B_ν , and consequently the self-emission term, becomes negligible, Eq. 1 becomes:

$$\frac{dI_\nu}{ds} = -k'_\nu I_\nu \quad (3)$$

Solving for I_ν , Eq. 3 becomes:

$$I_\nu(s) = I_{\nu, start} e^{-\int k'_\nu ds} \quad (4)$$

the ideal case of backlighting. In this equation $I_{\nu, start}$ is the spectral intensity emitted by the backlighter source, and the integral of $k'_\nu ds$ is the optical depth. Since k'_ν is consistently large inside the target shell and approximately zero outside, the optical depth depends mainly on the distance of x-ray travel through the shell. Therefore, the optical depth is almost 0 for rays starting at A, intermediate at B, and large at C (Fig. 5). Unfortunately, the local temperature on the x-ray path can reach up to several thousand electron volts, causing self-emission to become a significant factor.

To solve Eq. 1, $I_{\nu, start}$ needs to be known. It can be parameterized as a function of the backlighter temperature T_{XR} :

$$I_{v,\text{start}} = B_v(T_{\text{XR}}). \quad (5)$$

Currently, 300 eV has been determined as a reasonable¹³ backlighter temperature.

2.2: Numerical algorithm for integrating an x-ray path

The x-ray is integrated along its path taking small steps of interval ds . Assuming that the temperature and opacity are constant on the interval, Eq. 1 can be rewritten as:

$$\frac{d(I_v - B_v)}{ds} = -k'_v(I_v - B_v) \quad (6)$$

since $dB_v/ds=0$. Integrating each side,

$$I_v(s + ds) - B_v = (I_v(s) - B_v)e^{-\int k'_v ds} \quad (7)$$

is obtained. This gives the spectral intensity at the new position:

$$I_v(s + ds) = I_v(s) * e^{-k'_v ds} + B_v(s)(1 - e^{-k'_v ds}). \quad (8)$$

As in Eq. 1, the first term of Eq. 8 on the right hand side represents the absorption while the second term represents the self-emission. Eq. 8 maintains the assumption that the spectral emission occurring during an interval of x-ray travel ds is defined by Eq. 2 for the local temperature and opacity at the beginning of the interval. Since the temperature and opacity can change quickly, especially when the x-ray is near the shell of the target, a small ds needs to be used to accommodate this assumption. Convergence is achieved once the ds is small enough that an image created with a value ds and another image created with a value $\frac{1}{2}ds$ are almost indistinguishable.

3. Solutions for 1-D hydrodynamic profiles:

3.1: Introduction of 1-D hydrodynamic profiles

In order to solve Eq. 8, the opacity and B_v need to be known. For the ideal case of a spherically symmetric shell, the temperature and density profiles can be obtained from a 1-D

hydrodynamic code such as LILAC. LILAC provides densities and temperatures as a function of radius R, the distance from the target center (Fig. 6). In Fig. 6, the target shell is between 400 and 500 microns in radius. On the right side of the high density spike, the outside of the shell is hot from the lasers striking the surface. Inside the shell (left), the DT has a low density, and is

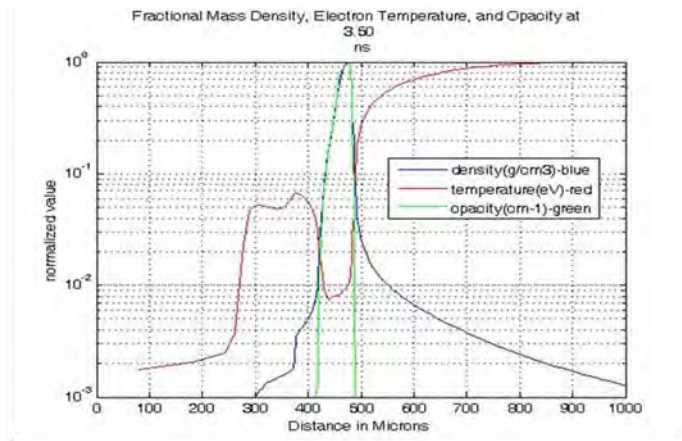


Figure 6: A LILAC plot showing the normalized density, temperature, and opacity versus radius at the end of the laser pulse. The blue line represents density, the red line represents temperature, and the green line represents opacity. The opacity is proportional to the density inside the shell because the temperature is low. The target shell is now between 400 and 500 um in radius, halfway from the initial radius of 865 um.

heated by energy from the shock propagating inwards. Since the curves of density and temperature versus radius are smooth, the density and temperature of any given radius can be found using linear

interpolation. One of the quantities needed to solve Eq. 8

is opacity, k'_ν . This is provided by

data from the Los Alamos Astrophysical Opacity Library,¹⁴ giving opacity as a function of density, temperature, and frequency. Therefore, for any given x-ray with a known frequency and radius R, the opacity can be found using interpolation with respect to the density,

temperature, and frequency. The other quantity needed to solve Eq. 8, B_ν , is a function of the temperature and frequency.

A plot superimposing opacity, temperature, and self-emission, or $k'_\nu B_\nu$, versus radius clearly illustrates the relationship

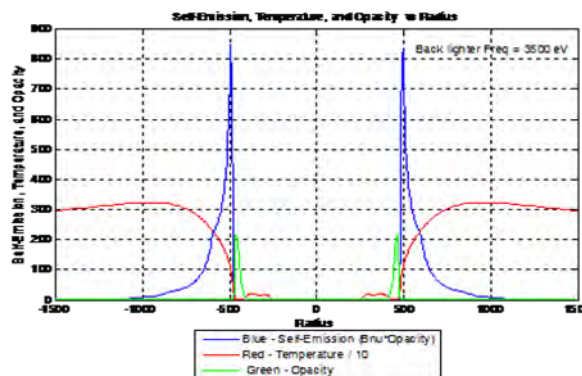


Figure 7: Self-emission (blue), temperature (eV/10, red), and opacity (1/cm, green) versus radius. The self-emission reaches a maximum just outside the shell. The opacity and self emission are used by *Blackthorn* to solve Eq. 8.

between the three values (Fig. 7). The opacity is high for the shell, where the temperature and self-emission are low. The self-emission reaches a maximum just outside the shell when the temperature is still moderately high. Self emission drops inside the target because the inside of the target is cool relative to the hot shell. As the radius increases, the self-emission also decreases due to a decrease in opacity.

3.2: Predicted backlighting for 1D target profiles

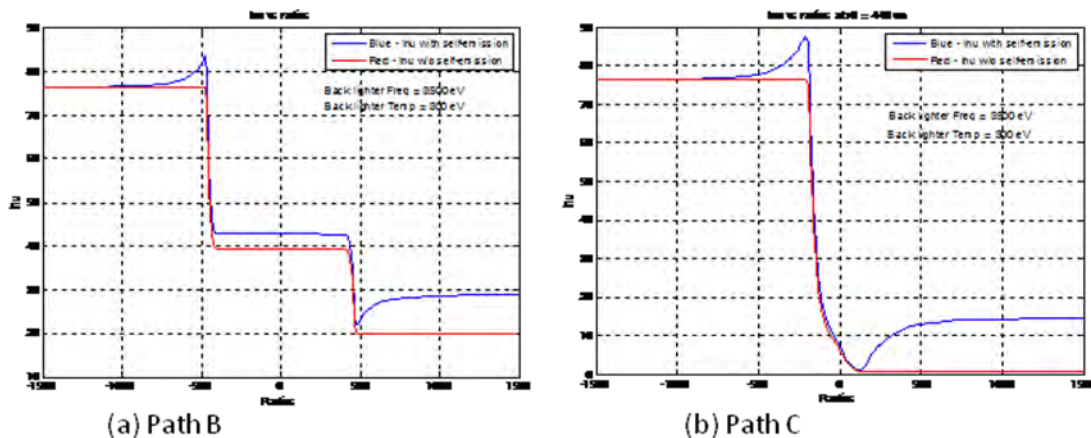


Figure 8: Spectral intensity versus the distance along the path of for an x-ray going through the center of the target (a) and starting at a distance $u = -440 \mu\text{m}$ away from the center of the target, near the edge of the shell (b) with (blue) and without (red) self-emission. (a) corresponds to the x ray B and (b) corresponds to the x ray C in Fig. 5. Self emission increases the spectral intensity whenever the x ray is just outside the target shell.

Fig. 8 shows graphs of spectral intensity versus distance s along the x-ray paths B and C of Fig. 5a, containing superimposed curves of the spectral intensity with and without self-emission. Figure 8a displays rays passing through the center of the target and Fig. 8b rays closest to the edge of the target shell. In both cases, the self emission increases the spectral intensity directly outside the target shell and after it passes completely through the target. Since the x-ray in Fig. 8b has a longer portion of its path inside the shell, more absorption occurs, and less intensity emerges from the target.

To predict what experimentalists would see on the backlighting images, Fig. 5b shows graphs of spectral intensity versus radius in the image plane with and without self-emission. The

transmission begins to rapidly drop just inside the outer radius of the target shell and reaches a minimum at the edge of the inner radius of the shell. This allows the backlighting image to reveal the inside and outside edges of the target. Self-emission increases the spectral intensity shown on the backlighting image inside the target and creates an increase of the spectral intensity to values above $I_{v,start}$ around the outside edge of the target. However, the self-emission in Fig. 5b does not affect the location of the inner or outer edges of the shell.

3.3: Frequency Optimization

To find an optimal frequency, superimposed plots of transmission versus radius in the image plane for different x-ray frequencies can be used (Fig. 9). Fig. 9 is similar to Fig. 5b, but

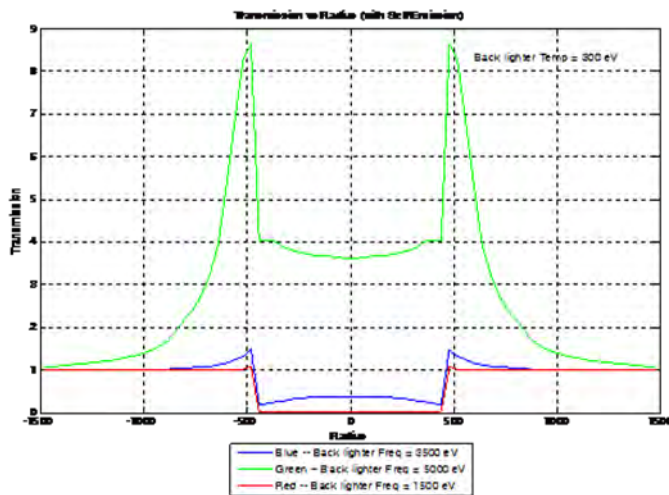


Figure 9: Transmission vs. radius in the image plane calculated at different frequencies. The green line represents a frequency of 5000 eV, the blue line 3500 eV, and the red line 1500 eV. An image using the 5000 eV frequency would become dominated by self-emission, and an image using the 1500 eV frequency would show almost no self-emission. However, neither frequency provides information about the inside of the target.

dramatically for the x-ray source than the plasma, so $I_{v,start}$ is greatly reduced for higher x-ray frequencies. In this case, the target becomes dominated by self-emission, as shown by the curve representing an x-ray frequency of 5000 eV. The minimum transmission inside the target becomes 3.5, and the maximum transmission, caused by the x-rays that are skimming the

instead of spectral intensity (I_v), the transmission, $I_{v,final}/I_{v,start}$ is plotted. The transmission depends strongly on the x-ray frequency.

As the x-ray frequency increases, the value of the exponential in Eq. 2 also increases, and would result in a lower B_v in the plasma and a lower $I_{v,start}$. This exponential term changes much more

outside of the shell, is more than 8.5. At the other extreme, shown by the curve with an x-ray frequency of 1500 eV, the transmission inside the shell is consistently close to zero. The shape of this curve is similar to the transmission curve with no self-emission (red) shown in Fig. 5b.

Having too high or too low of an x-ray frequency is problematic because in both cases there is a lack of information about the inside of the shell. In the 5000 eV case, the image would be created primarily by the target's self emission. On the other hand, for the 1500 eV x-rays, the x-rays are so strongly attenuated that little energy reaches the inside of the target, so x rays don't fully penetrate the target and emerge with sufficient energy to provide details about the inside. The 3500 eV x-rays create a curve that comes closest to the ideal transmission curve; the transmission is 1 outside the target (except the regions directly outside the target slightly affected by self-emission), and the transmission curve reaches a minimum just inside the shell and increases towards the center, following the limb effect. Therefore, a frequency of 3500 eV has been temporarily chosen.

3.4: Images taken after the end of the laser pulse

The backlighting image can also be taken after the laser pulse has been turned off. This can be simulated by using a temperature factor, wherein all the temperatures obtained from the LILAC profile are multiplied by this factor in order to mimic the cooling of the target over

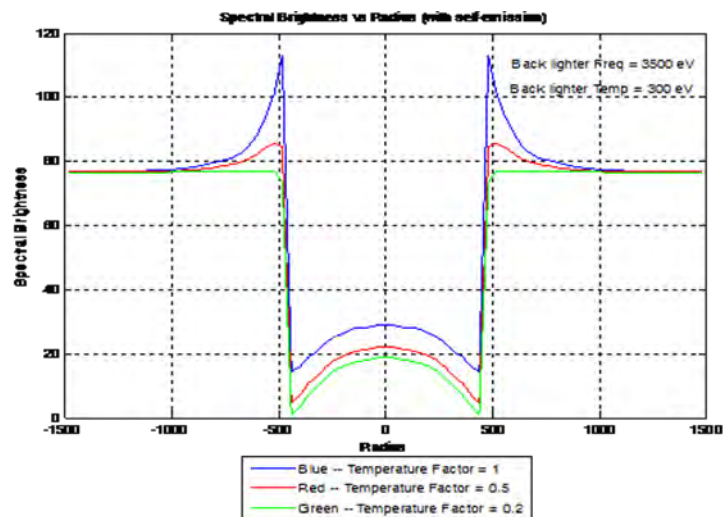


Figure 10: Spectral intensity versus radius in the image plane with the temperature multiplied by factors of 1 (blue), 0.5 (green), and 0.2 (red). As the temperature factor decreases, the effect of self emission, and also the spectral intensity, decreases. Therefore, images taken just after the laser turns off would show less self-emission.

time after the laser pulse has ended. A 1-D plot of spectral intensity versus radius in the image plane with superimposed plots with three different temperature factors can be used to analyze the effects of cooling (Fig. 10). The temperature factors used are 1, 0.5, and 0.2, simulating the target 0, 0.35, and 0.85 nanoseconds after the laser pulse has been shut off. As the temperature factor decreases, the transmission maxima decrease, signifying that the amount of self-emission also decreases. Once the temperature factor is as low as 0.2, almost no self-emission is shown, shown by the flat spectral intensity outside of the target. In addition, a much clearer minimum just inside the shell can be seen. Therefore, images taken after the laser pulse should be better than those taken during the pulse. To adjust for this advantage, the laser pulse could possibly be switched off slightly earlier to obtain self-emission-free images for more times.

4. Modeling of 3D target profiles

Each target position can be represented by a spherical angle (θ, Φ) where θ is the angle clockwise from the positive z-axis and Φ is the angle clockwise from the x-axis in the x-y plane. As described by Tucker¹⁰, the computer code SAGE calculates the center of mass radii for positions all around the target as a function of (θ, Φ) . Typical plots of the center of mass radii are

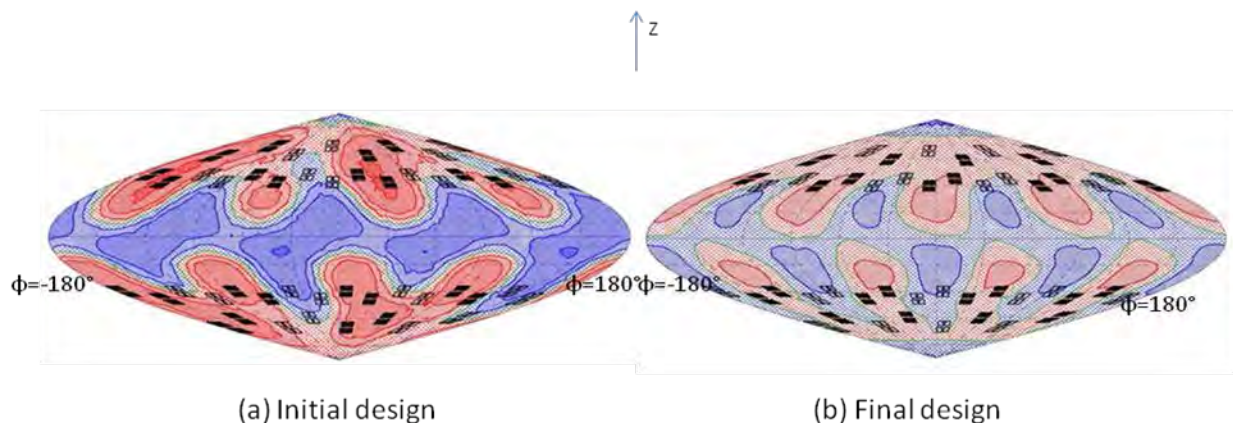


Figure 11: SAGE plots of Tucker's initial and final designs displaying the center of mass radius of the target. The black quads are those that are used to implode the target. The projection maps the whole sphere to the plane and displays radius as a function of the spherical angle (θ, Φ) . The rms variation of 22 μ m in the initial design was reduced to 8 μ m in the final design. (from Ref. 8)

shown in Fig. 11 for Tucker's initial and final designs. Red areas represent areas that are over-compressed, while blue areas represent ones that are under-compressed. The darker the color is, the more over/under compressed the area is. In both (a) and (b), the equatorial positions are compressed less than the polar positions. However, it is obvious that the initial design shows a much greater difference in the compression between the polar and equatorial positions.

SAGE produces profiles similar to the LILAC profiles of density and temperature versus radius, but with less resolution, since SAGE is a 2D code. To compensate for the lower resolution, a LILAC profile can be

combined with the SAGE center of mass calculations by shifting the LILAC profiles in each direction (θ, Φ) to match the center of mass provided by SAGE. In the solutions described above for 1D

hydrodynamic profiles, calculations were made purely based on LILAC, where the radius used for interpolation was the distance R

from the current x-ray position to the center of the target (see Fig. 5a). For 3D targets, with an x ray at position (R, θ, Φ) , *Blackthorn* first finds the center of mass radius (r_{cm}) in the direction (θ, Φ) , and then calculates a new radius r_{new} to correspond with the LILAC profile using the equation:

$$r_{new} = (R - r_{cm}) + r_{max_density} \quad (9)$$

where $r_{max_density}$ is the radius in the LILAC profile corresponding to the maximum density. r_{new} is then used to interpolate for density, temperature, and opacity in LILAC. So, for example,

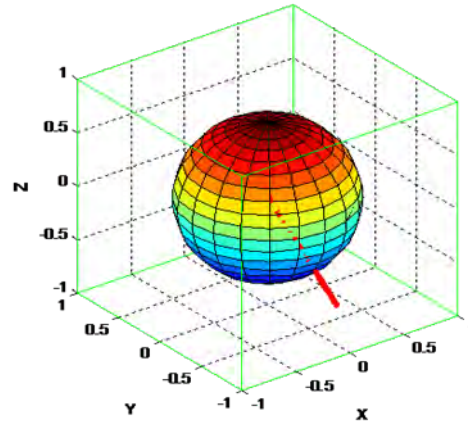


Figure 12: Grids on the six faces of a cube used to obtain r_{cm} as a function of direction (θ, Φ) . r_{cm} is stored at each grid point. For a direction given by the red line r_{cm} is found using bilinear interpolation at the point where the line intersects one of the grids.

whenever the x ray radius R is equal to r_{cm} , Eq. 9 will cause the LILAC values to be calculated at $r_{new} = r_{max_density}$. SAGE records the radii r_{cm} by creating a three-dimensional cube that encloses the target with grids, usually 20x20 or 30x30, on each of the 6 faces (Figure 12). This method is described in Ref. 15. At the center of each square on each grid is a grid-point at which the center of mass radius r_{cm} is stored. When the x ray moves to a new position (x,y,z) for which (R, θ, Φ) are calculated, *Blackthorn* finds the coordinates where the red line in the direction (θ, Φ) intersects one of the grids. Then, *Blackthorn* calculates r_{cm} in that direction using bilinear interpolation.

4.1: Selection of rays:

Given a viewing direction (θ, Φ) , a unit vector $c=(\sin(\theta)\cos(\Phi), \sin(\theta)\sin(\Phi), \cos(\theta))$ can be used to represent the direction of the camera and of x-ray travel with respect to the x,y,z axes. Using the components of the direction vector, an imaginary (u,v) plane, which is perpendicular to the direction of x-ray travel, can be created. The (u,v) plane is placed 1500 μm away from the target center and simulates the image plane (see Fig. 5a), where x-rays strike and form the image. The components of unit vectors in the u and v directions can be defined by $u_1=(-\sin(\Phi), \cos(\Phi), 0)$ and $v_1=(-\cos(\theta)\cos(\Phi), -\cos(\theta)\sin(\Phi), \sin(\theta))$. Given the coordinates of the x-ray starting position in the (u,v) plane, the unit vectors are used to find the starting coordinates in the (x, y, z) plane.

Blackthorn shoots rays in a polar fashion from the center of the (u,v) plane. The x-rays are first shot along the radial direction at angle of 0 with respect to the positive u -axis. This is repeated for the other angles. Polar ray tracing allows the curves of the contour plot to be smoother than the jagged curves resulting from a rectangular grid of x-rays. Therefore, it allows a much smaller number of rays to be used in order to reach convergence.

5. Predicted images for 3D target profiles

Two different camera angles are available on the NIF for viewing backlighting images. A

view from the pole position ($\theta=0, \Phi=0$) can be used to diagnose the azimuthal uniformity of the target

while a view from the equator

($\theta=90, \Phi=79$) can be used to diagnose the balance of compression between the polar and equatorial positions.

Fig. 13 shows a polar-view backlighting image of Tucker's initial design. The x-ray energy used is 3500 eV and T_{XR} is 300 eV. The yellow portion shows the outside of the target, where the transmission is 1. The orange ring indicates that the transmission is greater than 1, and is caused by self-emission from just

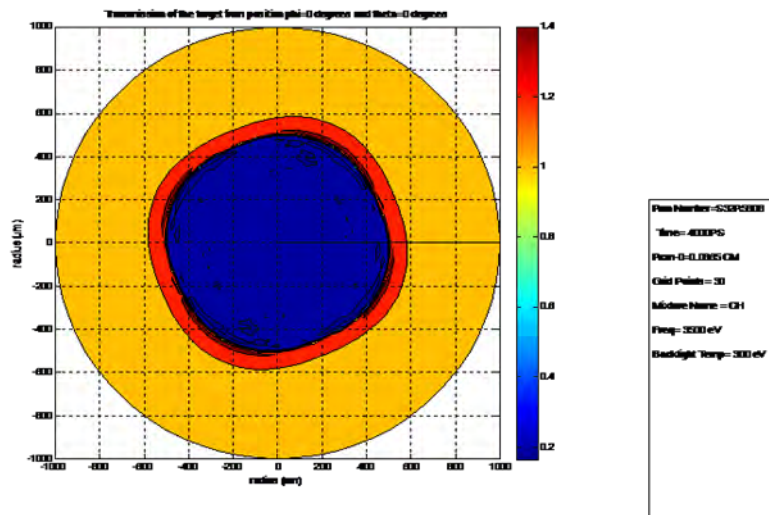


Figure 13: 2-D backlighting image of Tucker's original design from the polar view displaying contours of transmission. There is a four-fold pattern displaying structure around the edge and inside the target shell. The azimuthal uniformity is mediocre.

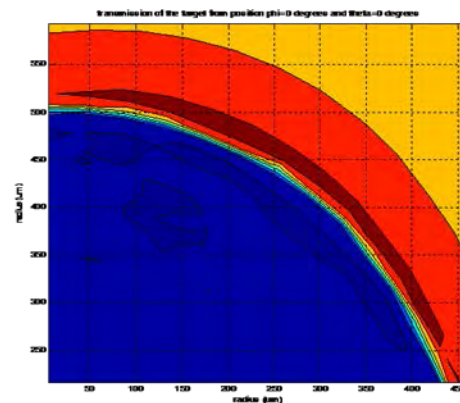


Figure 14: Zoomed in view of the upper right portion of the image shown in Fig. 13. It shows that in the black ring in Fig. 13, the transmission is rapidly transitioning from low to high.

outside the target's shell. The thin black ring shows the outer edge of the target's shell. Inside the black ring, the transmission rapidly transitions from the higher value outside the shell to the lower value inside (Fig. 14).

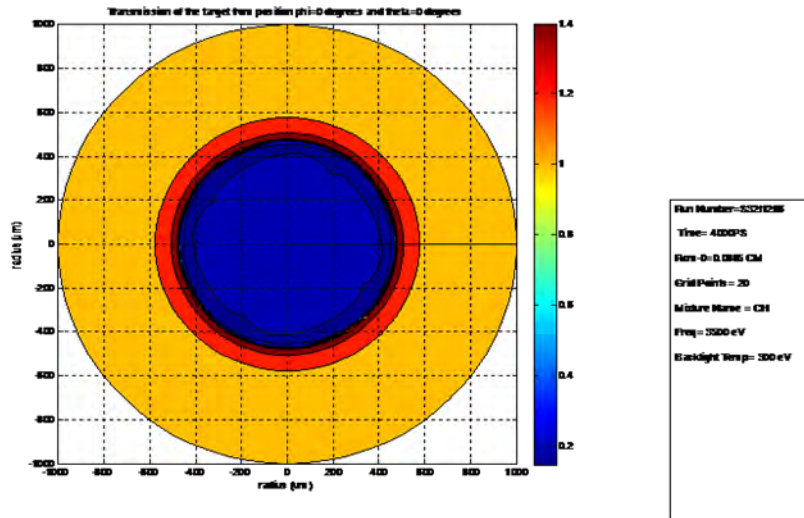


Figure 15: 2-D backlighting image of Tucker's final design from the polar view. The azimuthal uniformity has been greatly improved.

The image of Fig.13 shows a four-fold nonuniformity pattern around the outside ring of the target. The offset of the pattern from 0,90,180, and 270 degrees corresponds with the offset of the beams on the NIF equatorially (see Fig. 11). Slight nonuniformities can also be seen directly

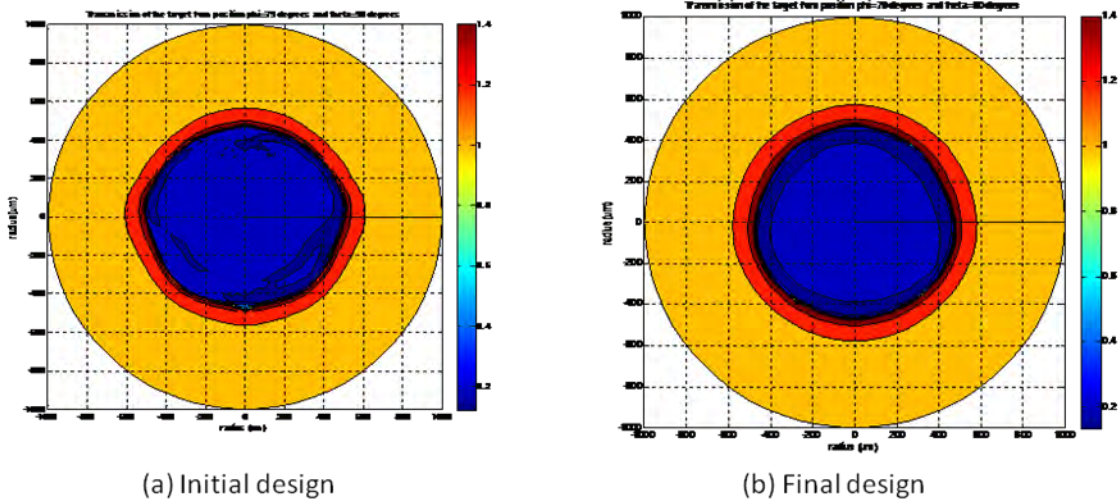


Figure 16: (a) 2-D backlighting image of Tucker's original design from the equatorial view. The equatorial positions are compressed less than the polar positions, and there is structure present inside the target shell. (b) 2-D backlighting image of Tucker's final design from the equatorial view. The equatorial positions are slightly less compressed than the polar regions. The structure has been reduced.

inside the ring, also in a four-fold pattern. When viewing Tucker's final design from the polar view (Fig. 15), the overall shape of the target is much more round. Most of the structure around the outside of the ring is eliminated. Some structure inside the ring, also in a four-fold pattern, can just be perceived.

In the equatorial view of Tucker's original design (Fig. 16a), it is clear that the equatorial positions are compressed much less than the polar positions. There is also a significant amount of structure directly inside the shell. In the equatorial view of Tucker's final design (Fig. 16b), the nonuniformity is much less, but the equatorial positions are still compressed slightly more. The inner structure has also been reduced.

Conclusion

A shock-ignition experiment has been proposed for the National Ignition Facility. To model x-ray backlighting of targets for these experiments, a computer code *Blackthorn* has been written. *Blackthorn* combines a 1-D LILAC profile with 3-D SAGE predictions to create 1-D plots of x-ray intensity and 2-D backlighting images that can be used to diagnose the uniformity of target compression. *Blackthorn* can also help optimize the x-ray frequency, backlighter temperature T_{XR} , and times to take the backlighting images. The exact T_{XR} will depend on the number of beams used for backlighting and the material of the backlighting source. *Blackthorn* determined that 3500 eV is an optimal frequency to form backlighting images, which should be taken just after the laser pulse has been turned off to reduce the effects of self-emission. *Blackthorn* shows a clear distinction between optimum designs, like Tucker's design which produces very spherical images, and non-optimum designs, which produce clearly nonuniform images, enabling nonuniform implosions to be diagnosed. *Blackthorn* can thus be used in support of research on the NIF towards the possibility of obtaining fusion energy using shock-ignition.

Acknowledgements:

I would like to thank Dr. Craxton for inviting me to the summer program, taking time to advise my project, and supporting me during and after the program. I would also like to thank Laura Tucker for aiding my research with a more optimized capsule design.

References:

1. J.D. Lindl, "Development of the Indirect-Drive Approach to Inertial Confinement Fusion and the Target Physics Basis for Ignition and Gain," *Phys. Plasmas* **2**, 3933 (1995).
2. J Nuckolls et al., "Laser Compression of Matter to Super-High Densities: Thermonuclear (CTR) Applications," *Nature* **239**,139 (1972).
3. S. Skupsky et al., " Polar Direct Drive on the National Ignition Facility ", *Phys. Plas* **11**, 2763 (2004)
4. R.S. Craxton et al., "Polar Direct Drive : Proof-of-Principle Experiments on OMEGA and Prospects for Ignition of the National Ignition Facility," *Phys. Plas* **12**, 056305 (2005)
5. A.M. Cok, "Development of Polar Drive Designs for Initial NIF targets," LLE Summer High School Research Program (2006)
6. S. Atzeni and J. Meyer-ter-Vehn, "The Physics of Inertial Fusion," Clarendon (2004).
7. L.J. Perkins, et al., "Development of a Polar Drive Shock Ignition Platform on the National Ignition Facility," NIF Facility Time Proposal (2010).
8. R. Betti et al., "Shock Ignition of Thermonuclear Fuel with High Areal Density," *Phys. Rev. Lett.* **98**, 155001 (2007)
9. L.J. Perkins et al., "Shock Ignition : A New Approach to High Gain Inertial Confinement Fusion on the National Ignition Facility,"*Phys. Rev. Lett.* **103**, 045004 (2009)
10. L. Tucker, "A Design for a Shock Ignition Experiment on the NIF Including 3-D Effects," LLE Summer High School Research Program (2010)

11. R.S. Craxton and R.L. McCrory, "Hydrodynamics of Thermal Self-Focusing in Laser Plasmas," J. Appl. Phys. **56**, 108 (1984).
12. Ya. B. Zel'dovich, Yu. P. Raizer, "Physics of Shock Waves and High-Temperature Hydrodynamic Phenomena, " New York: Academic Press (1966-1967)
13. R. Epstein, Discussion about backlighting temperature, 11 October 2010
14. W.F. Huebner et al., " Astrophysical Opacity Library, " Los Alamos Scientific Laboratory Report LA-6769-M (1977)
15. G. Balonek, "How good is the Bright Ring Characterization for Uniformity of Deuterium Ice Layers Within Cryogenic Nuclear Fusion Targets?," LLE Summer Program (2004)